Explicit Reference Governor for Constrained Maneuver and Shape Control of a Seven-State Multibody Aircraft

Ian O'Rourke, Ilya Kolmanovsky, and Anouck Girard* University of Michigan, Ann Arbor, MI, 48109

Emanuele Garone[†] *Université Libre de Bruxelles, Bruxelles, Belgium*

A combination of a Linear Quadratic Integral (LQ-I) controller for trajectory and shape control and an Explicit Reference Governor (ERG) for constraint satisfaction is used to provide constrained control for a longitudinal, nonlinear, multibody, seven-state Very Flexible Aircraft (VFA) model. The ERG works directly with the nonlinear model to provide a safe reference command input for the LQ-I controller, which tracks set-points in the aircraft velocity, angle of attack, pitch angle, and multibody dihedral angle, that allows the resulting trajectory to remain within the constrained region. This paper described the development of the LQ-I and ERG control combination, and the feasibility of this approach without and with a simple turbulence model, and comparisons to a similar Scalar Reference Governor (SRG) control scheme, based on simulations of pitching maneuvers of the aircraft with constraint enforcement on both the state vector and control parameters.

I. Introduction

Very Flexible Aircraft (VFA) can be challenging to control. Their long wings, with relatively low stiffness when compared to more traditional aircraft, result in highly nonlinear dynamics, which change significantly throughout maneuvers. These aircraft may be so flexible that structural concerns arise during maneuvers, where large loads may be placed on aircraft structures. Active constrained control of this flexibility is desirable to obtain high efficiency of the system and to avoid exceeding the structural limits of the aircraft; however, this problem is difficult due to the inherently nonlinear dynamics associated with flexible aircraft as the wing deformation changes.

Similar problems have been studied and various approaches tested in literature in order to provide this active control. Model predictive control has been used for gust load alleviation and constraints for flexible and very flexible aircraft in [1] and [2]. A trajectory control problem has been studied in [3] using a high-order model in UM/NAST without gusts, with gusts being added in [4]. The use of multiple control loops for each shape control and trajectory control has also been studied in [5]. Scalar Reference Governors (SRG) have been used in [6] to provide constraints of the root curvature during maneuvers of a UM/NAST model.

Outside of constrained control, [7] and [8] describe a small seven-state nonlinear, longitudinal model for a VFA. This model uses several rigidbody aircraft joined together through joints, creating a multibody aircraft, as opposed to a true flexible wing with a smooth surface. This model is used to analyze a linear controller and an adaptive Linear Quadratic Gaussian (LQG) / Loop Transfer Recovery (LTR) controller. In [8], a simple turbulence model based on a normal random distribution of velocities is used to look at the effect of noise on a controller that does not include the dihedral angle as one of the measured states.

These two ideas are combined in [9], where the model from [7] is combined with a SRG, as described in [10] and [11], and a Linear Quadratic Integral (LQ-I) controller. This allowed for both maneuver load alleviation, trajectory control, and shape control on the original nonlinear model.

In this paper, we extend the work done in [9] to an Explicit Reference Governor (ERG), as described in [12] and [13]. An LQ-I controller, created about a linearization of the model from a steady state trajectory, tracks set-points in the angle of attack, pitch angle, velocity, and dihedral angle, using the thrust, and deflections of the inner and outer ailerons and elevators as control inputs. The ERG maintains the constraints and adjusts the reference provided to the LQ-I controller in order to prevent constraint violations. Like the SRG, this allows for reduced computation requirements, as noted in [11] and [9], but provides better constraint control at set points further from the original steady state trajectory that the

^{*}Department of Aerospace Engineering, University of Michigan, Ann Arbor, MI

[†]Université Libre de Bruxelles, Bruxelles, Belgium

LQ-I controller is initialized about than the SRG. We present findings on the LQ-I controller and ERG combination and some comparisons to the SRG results in [9], as well as look at the effects of the simple wind model from [8] on the ERG.

We first provide an overview of the aircraft model in Section II, the LQ-I controller in Section III, and the ERG in Section IV. Then, we look at the combination of the LQ-I controller and ERG at a small, initially stable, dihedral angle steady state trajectory in Section V, and a larger, initially unstable, dihedral steady state trajectory in Section VI. We also present a simple wind turbulence model and the performance of the ERG under this stochastic response in Section VII. Finally, we present our conclusions in Section VIII.

II. Nonlinear Multibody Aircraft Model

The longitudinal nonlinear model for the VFA aircraft is obtained as derived in [7], which provides a three-body aircraft, where flexibility is provided by hinges at the rigid-body joints. This provides a simple, six-state model with five control inputs, which represents the wing flexibility with a single number as the dihedral angle η . As done in [9], the altitude state originally included in [7] has been removed to ensure that the overall system remains observable. Overall, the six states are provided as

$$X = \begin{bmatrix} V & \alpha & \theta & q & \eta & \dot{\eta} \end{bmatrix}^T, \tag{1}$$

where V is the aircraft velocity in ft/s, α is the angle of attack in radians, θ is the pitch angle in radians, q is the pitch rate in radians/s, η is the dihedral angle in radians, and $\dot{\eta}$ is the dihedral angle rate in radians/s. The five control inputs are provided as

$$U = \begin{bmatrix} \mathcal{T} & \delta_{a_c} & \delta_{a_o} & \delta_{e_c} & \delta_{e_o} \end{bmatrix}^T, \tag{2}$$

where \mathcal{T} is the overall thrust, δ_{a_c} is the inboard aileron deflection, δ_{a_o} is the outboard aileron deflection, δ_{e_c} is the inboard elevator deflection, and δ_{e_o} is the outboard elevator deflection. The thrust is in lbf and has a range between 0 and 200 lbf, and all deflections are angles in radians with ranges between -35° and 35° . This setup is depicted graphically in Fig. 1 for a front view showing the coordinate frames, and in Fig. 2 for a top-down view showing the control surfaces.

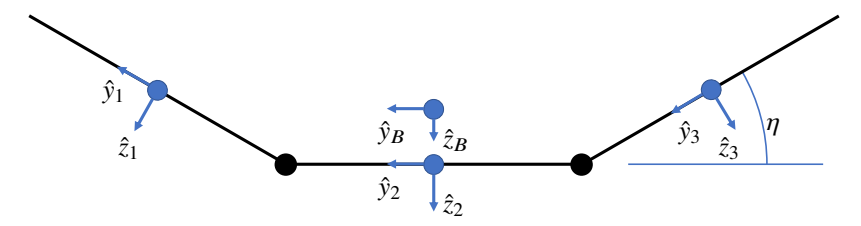


Fig. 1 VFA aircraft front view, showing all sectional coordinate frames (1, 2, and 3) and body coordinate frame (B), as in [7]. The \hat{x} direction for each coordinate frame is directed out front of the aircraft (out of the page).

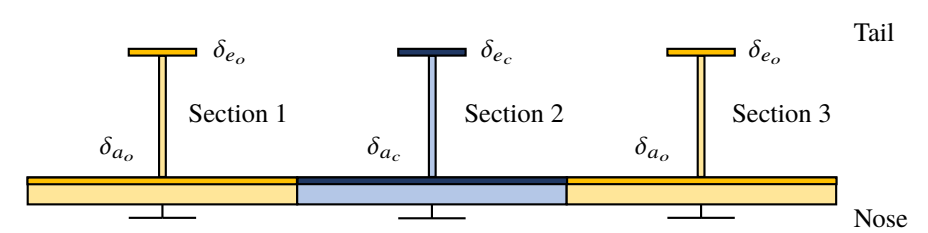


Fig. 2 VFA aircraft top-down view showing control surfaces at the rear of the wing and tail and propellers in the center towards the nose of each section.

The overall equations of motion are provided as

$$\dot{V} = (\mathcal{T}\cos\alpha - \mathcal{D})/m - g\sin\gamma, \quad \dot{\alpha} = -(\mathcal{T}\sin\alpha + \mathcal{L})/(mV) + q + g\cos(\gamma)/V,
\ddot{\eta} = \frac{\mathcal{H} - \kappa_c \dot{\eta} - \kappa_k \eta + d_1 - d_2}{d_3}, \quad \dot{q} = \frac{\mathcal{M} - 2c_2 \sin(\eta)\cos(\eta)\dot{\eta}q}{c_1 + c_2 \sin^2\eta},
\dot{\theta} = q,$$
(3)

with additional supporting terms provided in

$$c_{1} = 3I_{yy}^{*},$$

$$c_{2} = 2I_{zz}^{*} - 2I_{yy}^{*} + m^{*} \frac{s^{2}}{6},$$

$$d_{1} = \frac{s}{2} m^{*} \left((\dot{V} \sin(\alpha) V \cos(\alpha) \dot{\alpha}) \cos(\eta) - V \sin(\alpha) \sin(\eta) \dot{\eta} - \frac{2s}{3} \cos(\eta) \sin(\eta) \dot{\eta}^{2} \right),$$

$$d_{2} = (I_{yy}^{*} - I_{zz}^{*} - m^{*} \frac{s^{2}}{12}) \sin(\eta) \cos(\eta) q^{2} - \frac{s}{2} m^{*} \cos(\eta) V \cos(\alpha) q,$$

$$d_{3} = I_{xx}^{*} + m^{*} (\frac{s^{2}}{4} + \frac{s^{2}}{6} \cos^{2}(\eta)),$$
(4)

where \mathcal{D} is the drag, \mathcal{M} is the moment, \mathcal{H} is the hinge moment, γ is the flight path angle defined by

$$\gamma = \theta - \alpha,\tag{5}$$

and $\mathcal M$ is the moment about the $\hat y_B$ axis. All other constants are provided in Table 1.

Table 1 Constants for the aircraft model dynamics equations

Parameter	Symbol	Quantity	
Sectional Mass	m^*	9.32 slugs	
Sectional Inertia	I_{xx}^*	280 slugs . ft ²	
	I_{yy}^*	18.63 slugs . ft ²	
	I_{zz}^*	167.7 slugs . ft ²	
Sectional Span	S	80 ft	
Gravitational Acceleration	g	32.2 ft/s^2	
Dihedral Joint Damping	κ_c	141400 lbf/s	
Dihedral Joint Stiffness	κ_k	4900 lbf	

We then calculate the values for \mathcal{L} , \mathcal{D} , and \mathcal{M} through aerodynamic equations. Velocities u_i , v_i , and w_i represent the velocity along each of the axes for section i along axis \hat{x}_i , \hat{y}_i , and \hat{z}_i respectively, which are obtained for the middle section 2 and outer sections 1 and 3 from the states in X as

$$u_{2} = V \cos \alpha + q \frac{s}{3} \sin \eta, \qquad u_{3} = u_{1} = V \cos \alpha - q \frac{s}{6} \sin \eta,$$

$$v_{2} = 0, \qquad v_{3} = -v_{1} = (V \sin \alpha + \dot{\eta} \frac{s}{3} \cos \eta) \sin \eta,$$

$$w_{2} = V \sin \alpha + \dot{\eta} \frac{s}{3} \cos \eta, \quad w_{3} = w_{1} = (V \sin \alpha + \dot{\eta} \frac{s}{3} \cos \eta) \cos \eta - \dot{\eta} \frac{s}{2}.$$
(6)

This provides

$$V_i = \sqrt{u_i^2 + v_i^2 + w_i^2} \tag{7}$$

as the total velocity

$$\alpha_i = \arctan \frac{w_i}{u_i}, \quad \beta_i = \arcsin \frac{u_i}{V_i}$$
 (8)

as the sectional angle of attack α_i and sideslip angle β_i , and

$$Q_i = \frac{1}{2}\rho V_i^2 \tag{9}$$

as the sectional dynamic pressure Q_i with the atmospheric density ρ . This allows us to compute

$$\mathcal{L}_{w,i}^* = Q_i C_{\mathcal{L}_{w,i}} S_w^*, \qquad C_{\mathcal{L}_{w,i}} = C_{\mathcal{L}_{\alpha}} \alpha_i + C_{\mathcal{L}_{\delta}} \delta_{a,i}, \qquad (10)$$

$$\mathcal{D}_{w,i}^* = Q_i C_{\mathcal{D}_{w,i}} S_w^*, \qquad C_{\mathcal{D}_{w,i}} = C_{\mathcal{D}_0} + \kappa_{\mathcal{D}} C_{\mathcal{L}_{w,i}}^2$$
(11)

as the sectional wing lift $\mathcal{L}_{w,i}^*$ and drag $\mathcal{D}_{w,i}^*$ using the sectional wing lift coefficient $C_{\mathcal{L}_{w,i}}$ and drag coefficient $C_{\mathcal{D}_{w,i}}$. Other constants are outlined in Table 2. Similarly, we compute the same variables for the tail, with

$$\mathcal{L}_{t,i}^* = Q_i C_{\mathcal{L}_{t,i}} S_w^*, \qquad C_{\mathcal{L}_{w,i}} = C_{\mathcal{L}_{\alpha}} (\alpha_i + \delta_{e,i}), \qquad (12)$$

$$\mathcal{D}_{t,i}^* = Q_i C_{\mathcal{D}_{t,i}} S_w^*, \qquad C_{\mathcal{D}_{w,i}} = C_{\mathcal{D}_0} + \kappa_{\mathcal{D}} C_{\mathcal{L}_{t,i}}^2$$
(13)

as the sectional tail lift $\mathcal{L}_{t,i}^*$ and drag $\mathcal{D}_{t,i}^*$ using the sectional tail lift coefficient $C_{\mathcal{L}_{t,i}}$ and drag coefficient $C_{\mathcal{D}_{t,i}}$. All additional constants are outlined in Table 2.

Table 2 Constants for the aircraft model aerodynamic force equations

Parameter	Symbol	Quantity
Sectional Wing Reference Area	S_w^*	640 ft ²
Sectional Tail Reference Area	S_t^*	40 ft ²
Lift Coefficients	$C_{\mathcal{L}_{lpha}}$	2π
	$C_{\mathcal{L}_{\delta}}$	2
Parasitic Drag Coefficient	$C_{\mathcal{D}_0}$	0.007
Induced Drag Coefficient	$\kappa_{\mathcal{D}}$	0.07
Air Density at 40,000 ft	ρ	$5.8572 \times 10^{-4} \text{ slug/ft}^2$

We combine all the forces together into a single expression

$$P_{i}^{*} = \begin{bmatrix} -\mathcal{D}_{i}^{*} \\ 0 \\ -\mathcal{L}_{i}^{*} \end{bmatrix} = \begin{bmatrix} -(\mathcal{D}_{w,i}^{*} + \mathcal{D}_{t,i}^{*}) \\ 0 \\ -(\mathcal{L}_{w,i}^{*} + \mathcal{L}_{t,i}^{*}) \end{bmatrix}$$
(14)

that can be used with a local rotation matrix

$$R_{b/w}(\alpha, \beta) = \begin{bmatrix} \cos \alpha \cos \beta & -\cos \alpha \sin \beta & -\sin \alpha \\ \sin \beta & \cos \beta & 1 \\ \sin \alpha \cos \beta & -\sin \alpha \sin \beta & \cos \beta \end{bmatrix}$$
(15)

to convert between the local wind frame to the local section frame. The center section is already in the correct orientation for the overall rigid body frame, as shown in Fig. 1; however, the outer section frames must be rotated into the overall body frame using another rotation matrix

$$R_{2/1} = R_{2/3}^{T} = \begin{bmatrix} 1 & 0 & 0 \\ 0 & \cos \eta & \sin \eta \\ 0 & -\sin \eta & \cos \eta \end{bmatrix}$$
 (16)

where $R_{2/1}$ is used to convert from frame 1 to frame 2 and $R_{2/3}$ is used to convert from frame 3 to frame 2. Overall lift and drag becomes

$$\begin{bmatrix} -\mathcal{D} \\ 0 \\ -\mathcal{L} \end{bmatrix} = R_{b/w}(\alpha, \beta)^T \left(R_{2/1} R_{b/w}(\alpha_1, \beta_1) P_q^* + R_{b/w}(\alpha_2, \beta_2) P_w^* + R_{2/3} R_{b/w}(\alpha_3, \beta_3) P_3^* \right). \tag{17}$$

From these overall forces, we compute the moments, similar to the forces for the wing and tail above, as

$$\mathcal{M}_i^* = Q_i C_{\mathcal{M}_i} c_w S_w^*, \qquad C_{\mathcal{M}_i} = C_{\mathcal{M}_0} + C_{\mathcal{M}_{\delta}} \delta_{a,i}$$
 (18)

with the aerodynamic sectional pitching moment \mathcal{M}_i^* , pitching moment coefficient $C_{\mathcal{M}_i}$, and other constants defined in Table 3. We then combine aerodynamic moment with the forces from the wing and the tail to obtain

$$\mathcal{M} = \sum_{i=1}^{3} (\mathcal{M}_{i}^{*} + l_{w,i} \mathcal{D}_{w,i}^{*} - l_{t} \mathcal{L}_{t,i}^{*})$$
(19)

as the overall moment \mathcal{M} using the wing and tail boom lengths l_w and l_t respectively. These constants are found in Table 3, and $l_{w,i}$ is found as

$$l_{w,1} = l_{w,3} = \left(\frac{s}{2} - \frac{s}{3}\right) \sin \eta,$$

$$l_{w,2} = -\frac{s}{3} \sin \eta.$$
(20)

Table 3 Constants for the aircraft model aerodynamic moment equations

Parameter	Symbol	Quantity
Moment Coefficients	$C_{\mathcal{M}_0}$	0.025
	$C_{\mathcal{M}_{\delta}}$	-0.25
Wing Chord	c_w	8 ft
Tail Span	s_t	20 ft
Tail Chord	c_t	2 ft
Tail Boom Length	l_b	36 ft

Finally, we calculate the hinge moment ${\cal H}$ as

$$\mathcal{H} = (\mathcal{L}_{w,1}^* + \mathcal{L}_{t,1}^*) - m^* g \cos \eta \cos \theta \tag{21}$$

using the lift components of section 1. Note that, due to symmetry of the model, this would be identical if using the section 3 instead.

III. LQ-I Controller

An LQ-I controller is used to provide the active feedback control of the system. This controller controls the system based on α , θ , V, and η , and actuates \mathcal{T} , δ_{a_o} (symmetrically), δ_{e_c} , and δ_{a_c} , as in

$$U = \begin{bmatrix} \mathcal{T} & \delta_{a_o} & \delta_{e_c} & \delta_{a_c} \end{bmatrix}^T, \qquad y = \begin{bmatrix} \alpha & \theta & V & \eta \end{bmatrix}^T, \tag{22}$$

for controlled actuators U and control feedback y. The other control surface, δ_{a_c} , be set as a constant based on its steady state value. As the LQ-I controller requires a linear system, we linearize the nonlinear dynamics about a steady state trajectory using V=30 ft/s and $\gamma=0^{\circ}$, obtained from α and θ using Eq (5). We also choose a value for η , for example, $\eta=5^{\circ}$. The initial α and δ_{e_c} is specified as

$$\alpha^{o} = 7.5^{\circ} + \eta/600,$$
 $\delta_{e_{o}}^{o} = 5^{\circ} - \eta/10,$ (23)

as is done in [7]. This allows all the equations to be solved using an iterative solver to find a unique solution where all parameters in \dot{X} equal 0, indicating a steady state trajectory with state and control inputs X^o and U^o , respectively.

We also linearize about this point to obtain linearized A and B matrices for a standard linear model. As done in [7], we calculate the required control inputs in U for a steady state trajectory for $\gamma = 0^{\circ}$, as well as the linearized system stability from the eigenvalues λ of the A matrix, both in Fig. 3. In general, increasing the dihedral angle decreases the system stability and pushes the real components of the eigenvalues in the positive-real direction, indicating a reduction in stability.

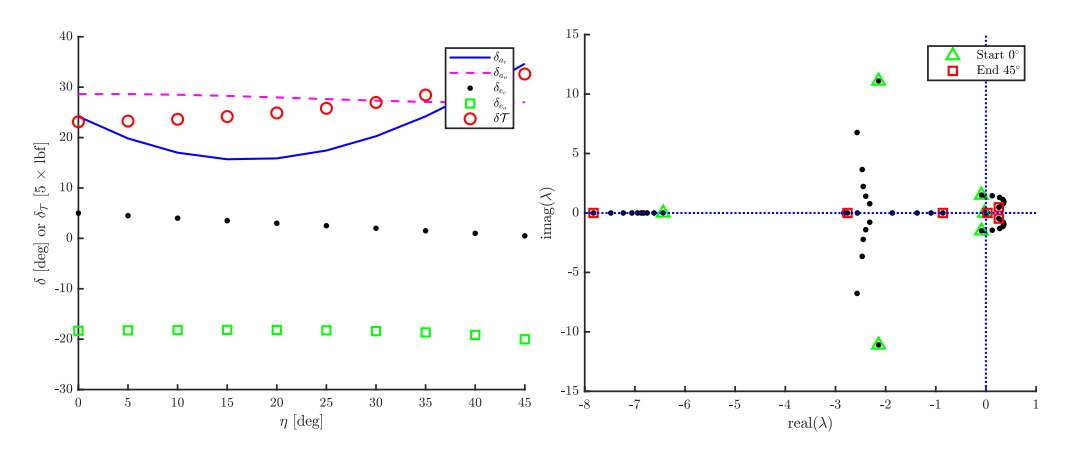


Fig. 3 The steady state trajectory control input values for dihedral angles between 0 and 45° in level flight (left), with corresponding linearized eigenvalues showing additional instability as the dihedral angle is increased for the same dihedral angles (right), show similar results to those found in [7].

From the chosen trajectories, we construct the linear model as

$$\dot{\tilde{X}} = A\tilde{X} + B\tilde{U}, \qquad \qquad \tilde{y} = C\tilde{X}, \tag{24}$$

where \tilde{X} , \tilde{U} , and \tilde{y} are the linear-model variants of their respective nonlinear system counterparts, obtained by

$$\tilde{X} = X - X^{o},
\tilde{U} = U - U^{o},
\tilde{y} = y - y^{o}.$$
(25)

The LQ-I design is obtained through applying LQR theory to the system, adding additional states to track the error between \tilde{y} and their commanded set-point values r,

$$\frac{d}{dt} \begin{bmatrix} \tilde{y} - r \\ \tilde{X} \end{bmatrix} = \begin{bmatrix} 0 & C \\ 0 & A \end{bmatrix} \begin{bmatrix} \tilde{y} - r \\ \tilde{X} \end{bmatrix} + \begin{bmatrix} 0 \\ B \end{bmatrix} \tilde{U} = \tilde{A}\tilde{X} + \tilde{B}\tilde{U}. \tag{26}$$

From LQR theory, we construct the weighting matrices for the state and control vectors as

$$Q = \operatorname{diag}([1000 \ 1000 \ 100 \ 100 \ 0.1 \ 0.1 \ 0.1 \ 0.1 \ 0.1 \ 0.1]), \tag{27}$$

$$R = \text{diag}([0.01 \quad 0.01 \quad 0.03 \quad 0.04]) \tag{28}$$

for the above \tilde{A} and \tilde{B} matrices. With these parameters, we obtain the LQ-I controller as

$$\tilde{U}(t) = KX_{cl} = \begin{bmatrix} K_i & K_p \end{bmatrix} \begin{bmatrix} z \\ \tilde{X} \end{bmatrix}$$
 (29)

for K as the LQR gain, with integral portion K_i and proportional portion K_p , and state error z obtained through

$$\dot{z} = \tilde{y} - r. \tag{30}$$

IV. Explicit Reference Governor

In order to provide a response to the nonlinear system dynamics, an Explicit Reference Governor (ERG) is one method that can be used in order to provide constrained control for the system. The ERG acts before the LQ-I controller, as in Fig. 4, where r is passed into the ERG, which then outputs a reference v that is used in the LQ-I controller instead of r directly. This allows the ERG to modify v to avoid constraint violation on the user-commanded r.

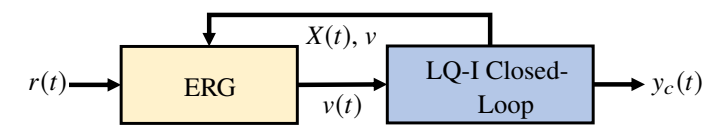


Fig. 4 ERG block diagram showing the user-input r(t), with the ERG acting and providing v(t) to the LQ-I controller and taking feedback of X(t) and v to make its modification.

The formulation of the ERG is as provided in [12]. Instead of working directly with v, the ERG works instead with \dot{v} . The goal of the ERG is to ensure that the resulting dynamics remain within the constraint bounds throughout the execution of the system. The overall problem for the ERG is

$$\dot{v} = \Delta(X, v)\rho(r, v). \tag{31}$$

The two primary parts to the ERG from Eq. (31) are the dynamic safety margin $\Delta(X, v)$ and the navigation field $\rho(r, v)$. The dynamic safety margin is a function that is strictly positive, such that $\Delta \geq 0$. Larger values for Δ denote that v is safer to change, and so thus result in a larger \dot{v} . This provides a value that correlates to how much, or rather how safe, it is to move the reference v towards r. The navigation field provides the vector in which to move v towards v.

A. Constraint Definition

We define the constraints used by the ERG as

$$Hy_c \le h,$$
 (32)

where H is the constraint output matrix, h is the constraint limit matrix, and y_c is the constraint output, obtained through

$$y_c = C_{\rm v} X,\tag{33}$$

for constraint output matrix C_y . For this problem, we pick C_y such that we get

$$C_{y} = \begin{bmatrix} \eta & \delta_{a_{o}} & \delta_{e_{c}} & \delta_{a_{c}} & \dot{\eta} \end{bmatrix}. \tag{34}$$

We can rearrange Eq. (32) into to provide a degree for how close the constraints are to their limit as

$$c = h - H y_c, \tag{35}$$

where c represents how close each constraint is to its limit. For each constraint value $c_i \ge 0$, the constraint i is satisfied, while $c_i < 0$ represents a constraint beyond its limit. This form of the equation proves to be more useful in the construction of the ERG.

B. Dynamic Safety Margin

One methodology to obtain a dynamic safety margin is through the use of Lyapunov theory, where there exists a Lyapunov threshold value $\Gamma(v)$ and a Lyapunov function V(X, v) to obtain $\Delta(X, v)$ as

$$\Delta(X, \nu) = \kappa \big(\Gamma(\nu) - V(X, \nu) \big), \tag{36}$$

$$\Gamma(v) = \frac{(-HX^o + h)^2}{H^T P^{-1} H},$$

$$V(X, v) = X^T P X,$$
(37)

where κ is a scalar positive constant and P is a positive-definite matrix, as in [12]. However, this approach is too conservative for this VFA system and often results in poor performance, especially when control surface deflections are

included in the constraints. Therefore, we look at the trajectory itself as the dynamic safety margin, where we propagate the system forward in time over some time horizon T_o to obtain the predicted states \hat{x} with the current reference v. From this, the minimum constraint value, as calculated in Eq. (35), is used as the dynamic safety margin. As the constraint equations provide negative values when outside of the constraints, a greater value represents states that are further away, and is "safer" than lower values. This comes from [12], and is

$$\Delta(X, \nu) = \kappa \min_{\tau \in [0, T_o]} \{ h - HC_y \hat{X}(\tau | X, \nu) \}, \tag{38}$$

where we have \hat{x} as the propagation of the system in time τ seconds into the future from the last value of X and v. This provides a method to obtain the degree of risk associated with moving the current v, with a larger minimum constraint value as "safer" to move than a smaller one. To improve controller performance, we also add a smoothing term

$$\sigma(v,r) = \min\left\{1, \frac{||r-v||}{\eta_s}\right\} \tag{39}$$

where η_s is a positive constant used to change the scale of this smoothing term, as is done in [13]. This term reduces the value of \dot{v} near the desired reference in order to reduce oscillations. We can then combine the smoothing and dynamic safety margin to get

$$\Delta_{smooth}(X, v) = \sigma(v, r)\Delta(X, v) \tag{40}$$

where $\Delta_{smooth}(X, \nu)$ is dynamic safety margin equation that we use in the ERG for the VFA aircraft. For this implementation, we use the full nonlinear model to propagate the state \hat{X} and a time horizon T_o of 10 s in Eq. (38). This performs well for these cases, but a better stopping criteria will be need to be researched.

C. Navigation Function

The navigation field for this problem is be derived simply as the normalized vector between r and v,

$$\rho(r, v) = \frac{r - v}{\max\{||r - v||, \eta_P\}},\tag{41}$$

obtained from [12]. We add a small, positive division tolerance term η_p so that, when v is very close to r, we avoid any division by zero.

V. Constrained Simulations with Small Dihedral Angles and ERG

For the first set of simulations, we want to see how the controller responds near the equilibrium point. We choose similar simulation points as in [9] so that we can compare the ERG response to that of the SRG. For the equilibrium point, we choose the steady state trajectory previously outlined, starting with a dihedral angle of $\eta = 5^{\circ}$. About these points, the linearized system has eigenvalues

$$\lambda_1 = -0.0207,$$
 $\lambda_{2,3} = -0.0308 \pm 1.4917i,$
 $\lambda_4 = -6.6181,$
 $\lambda_{5,6} = -2.5697 \pm 6.7663i,$
(42)

which all have negative real parts, indicating that the linearized open-loop system is stable; however, this doesn't tell too much about the nonlinear system, during which the stability changes throughout the maneuver. The simulations are run with a timestep $T_s = 0.01$ s, and in each simulation, the original steady state trajectory is held for 2 s before the new desired trajectory is provided to the controller in order to demonstrate the initial steady state trajectory. We also use constraints such that

$$4.5^{\circ} \le \eta \le 5.5^{\circ}, \quad 1.5^{\circ} \le \delta_{e_c} \le 7.5^{\circ},$$

 $25^{\circ} \le \delta_{a_c} \le 32^{\circ}, \quad 17^{\circ} \le \delta_{a_c} \le 23^{\circ}.$ (43)

For reference, Fig. 5 shows this simulation without the ERG. This shows significant angles beyond the provided constraints in nearly all constrained parameters.

We simulate the ERG with a command to set $\gamma = 5^{\circ}$, by setting $\theta_r = 13^{\circ}$ and $\alpha_r = 8^{\circ}$, resulting in Fig. 6. The ERG prevents significant excursions beyond the range of the constraints, unlike in the original unconstrained simulation,

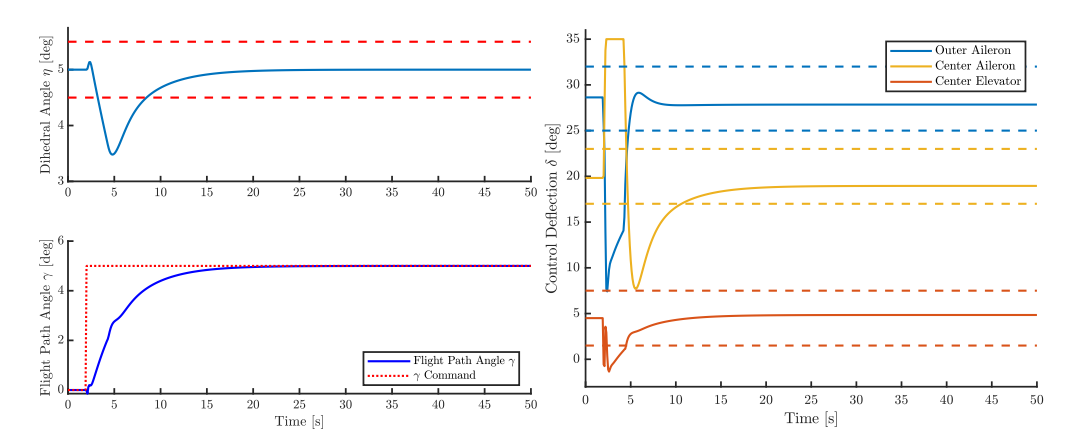


Fig. 5 Climb command without ERG increases the flight path angle to $\gamma = 5^{\circ}$, but violates constrains for all constrained parameters in both the dihedral angle and control surface deflections.

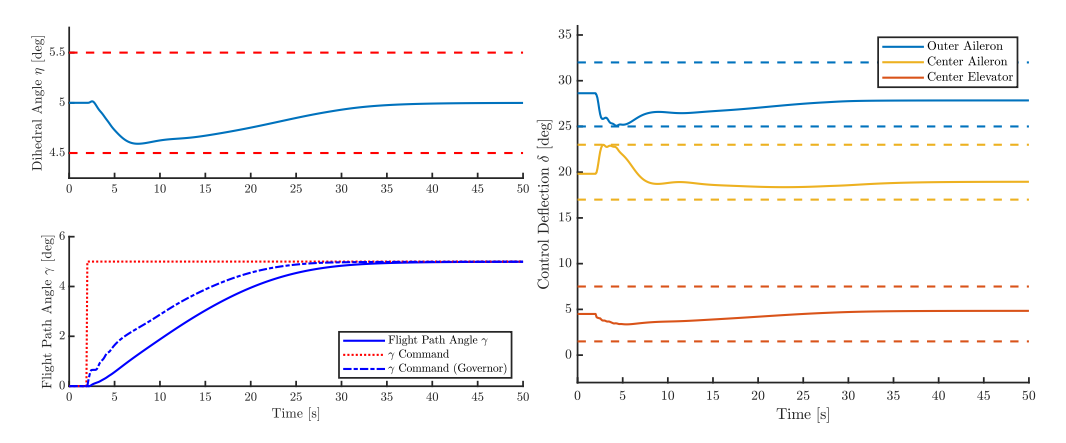


Fig. 6 Climb command with the ERG increases the flight path angle to $\gamma = 5^{\circ}$ without constraint violations, reaching the target flight path angle in about 35 s.

with the primary active constraints are the center and outer aileron. The ERG reaches the desired flight path angle in approximately 35 s. Note that the commanded γ is reconstructed from the reference commands for θ and α .

The ERG significantly impacts the results of the simulation by drastically reducing the magnitude of these constraint excursions and allows the aircraft to safely reach the commanded trajectory. We perform the same maneuver, this time with $\gamma = -5^{\circ}$, to illustrate the symmetry of the system in Fig. 7. In this case, there is also virtually no constraint violations as the controller again reaches the desired flight path angle in approximately 35 s.

Overall, these results show that the ERG is capable of preventing significant constraint excursions that would otherwise be present in the output of the closed-loop system. Looking at the stability of the system throughout a maneuver as determining the maximum real eigenvalue of the linearized open-loop A matrix at each of the flight conditions. Performing this for the first case, where we set $\gamma = 5^{\circ}$, we obtain Fig. 8. This shows that the controller does end up at an unstable equilibrium at $\gamma = 5^{\circ}$. While initially at a stable linearized system equilibrium point, the controller moves the nonlinear system smoothly to an unstable point at the desired $\gamma = 5^{\circ}$ with a maximum real-component eigenvalue of 0.017. This provides an indication of the degree of stability at each point along the trajectories from above from the actual nonlinear system.

We also run a similar test with $\gamma = 10^{\circ}$ to show how the ERG responds for a larger flight path angle command in Fig. 9. this shows a larger deviation from the steady state and illustrates one effect of the ERG in that there are oscillations that occur due to the fact that the reference ν is a dynamic system as well. It is subject to tuning of the ERG parameters, like κ , as well as the time step in the simulations.

When we compare these results with those from the linear SRG from [9], the SRG typically better maintains an active constraint, where one of the constraint terms is almost always right on the constraint limits. This is due to the

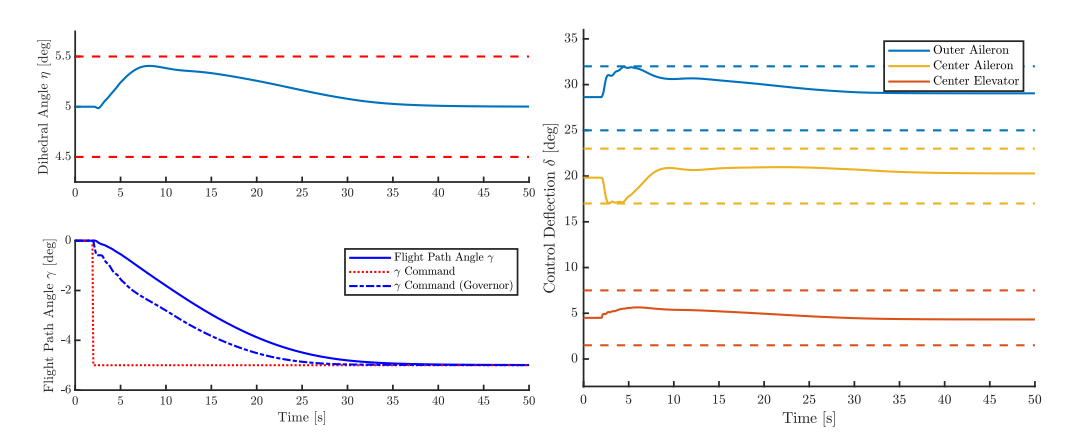


Fig. 7 Descent command with the ERG increases the flight path angle to $\gamma = -5^{\circ}$ without constraint violations, reaching the target flight path angle in about 35 s.

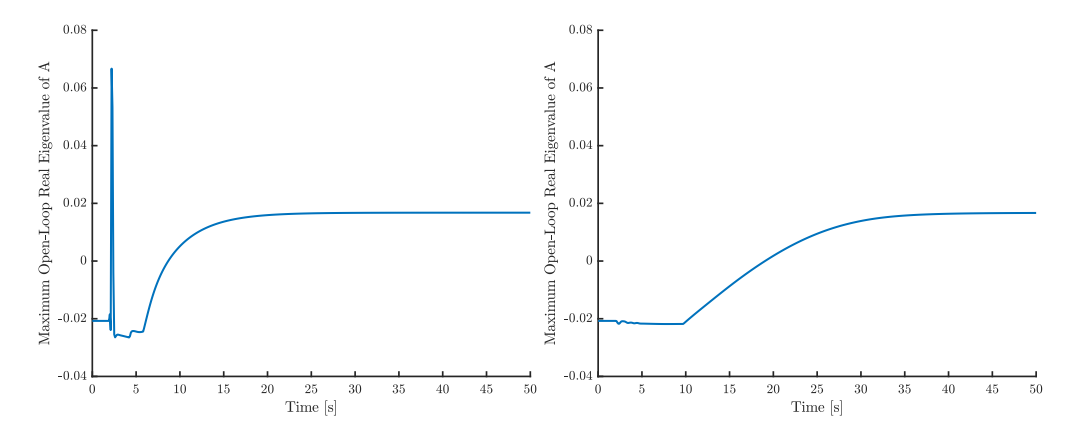


Fig. 8 Both without (left) and with (right) ERG for $\gamma = 5^{\circ}$ result in an unstable final trajectory; however, the without ERG has a sudden spike in the maximum real-component eigenvalue at the beginning, while no such spike occurs with the ERG and the system gradually increases to the final trajectory values.

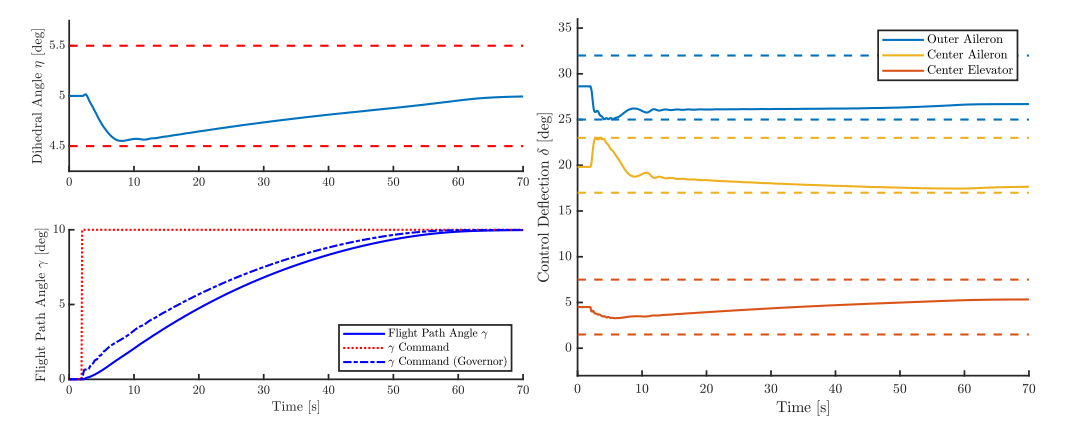


Fig. 9 Climb command with the ERG increases the flight path angle to $\gamma = 10^{\circ}$ without constraint violations, reaching the target flight path angle in about 65 s.

SRG solving an optimization problem on a scalar ratio κ between 0 and 1 to find the maximum possible value for ν based on the linearized system about the original trajectory propagated forward in time from the current state values. Because it is solving based on a linear system, this optimization can be done very rapidly. In comparison, the ERG adds

v as a dynamics term, so no optimization is done. Instead, the full nonlinear system is propagated and used as a guide for how close the trajectory would get to the constraints. This means that, while the ERG must be tuned, as it is an additional source for dynamics, and does not necessarily obtain the closest possible value for v to r at each time step, it is not dependent on the linear model and thus behaves more favorably in cases where the nonlinear dynamics diverge from the linearized dynamics about the equilibrium point. In these simulations, setting $\gamma = 5^{\circ}$ does not provide enough difference to allow the decrements in the SRG performance to allow the ERG to outperform; however, with the $\gamma = 10^{\circ}$ case, the ERG starts to outperform the SRG, reaching the desired flight path angle in a smooth fashion. For reference, the SRG output is shown in Fig. 10, which shows the decreasing performance of the SRG as the linear and nonlinear models diverge.

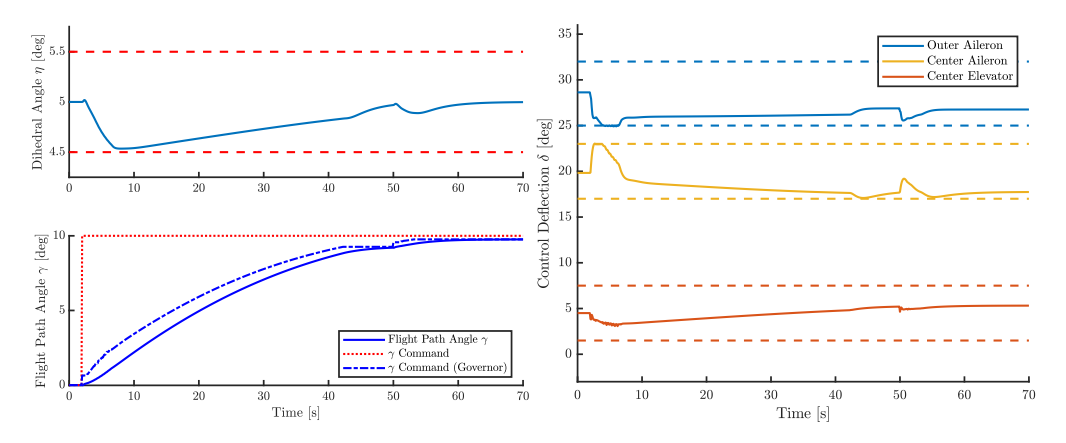


Fig. 10 Climb command with the SRG increases the flight path angle to $\gamma = 9.76^{\circ}$, nearly the target $\gamma = 10^{\circ}$, but results in a jagged climb command due to the linear model diverging from the nonlinear model at larger flight path angles.

VI. Constrained Simulations with Large Dihedral Angles and ERG

Increasing the dihedral angle further decreases the stability present in the system, as indicated in Fig. 3, which can become problematic for the LQ-I controller to counteract. At $\eta = 23^{\circ}$, we have linearized eigenvalues of

$$\lambda_1 = 0.0120,$$
 $\lambda_{2,3} = 0.3523 \pm 1.0421i,$ $\lambda_4 = -6.9121,$ $\lambda_{5,6} = -2.3515 \pm 1.0232i,$ (44)

which are clearly unstable based on λ_1 and $\lambda_{2,3}$ having positive-real components. In addition, the LQ-I controller is not able to stabilize this system alone, with the nonlinear dynamics diverging too much from the linearized dynamics used within the controller as the controller tries to reach the flight path angle without any knowledge of constraints or control surface saturation. For the new dihedral angle, we also add new constraints of

$$22^{\circ} \le \eta \le 24^{\circ}, \qquad -2.3^{\circ} \le \delta_{e_c} \le 7.7^{\circ},$$

 $22.76^{\circ} \le \delta_{a_o} \le 32.76^{\circ}, \quad 11.64^{\circ} \le \delta_{a_c} \le 21.64^{\circ}.$ (45)

Once the ERG is added, however, the system is able to be stabilized. The ERG prevents the controller from moving too quickly and enforces the constraints on the control surface and dihedral angle, and slowly moves the reference accordingly, to ensure that the LQ-I controller is not allowed to make too sudden of movements that would otherwise cause instabilities. This is shown in Fig. 11, where the target command of $\gamma = 10^{\circ}$ is reached in about 50 s without constraint violations.

In addition, we also test the behavior of the system when requesting a command that would require a control input beyond the given constraints in the steady state case. If we set $\gamma = 20^{\circ}$, the ERG is successful in preventing exceedances in this case in Fig. 12, with the controller only able to reach a maximum $\gamma = 14.33^{\circ}$ before the center aileron constraint is limited against its lower bound. The ERG successfully limits the controller from moving beyond this and maintains the constraint, settling into this lower-angle flight path.

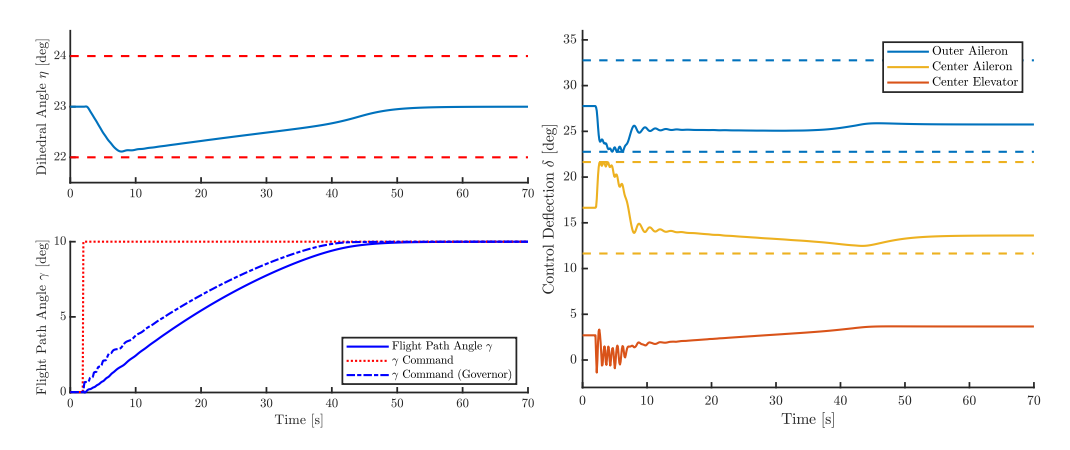


Fig. 11 ERG can stabilize the otherwise instable system at $\eta=23^{\circ}$ and targeting $\gamma=10^{\circ}$, and properly reach the desired target γ in about 50 s.

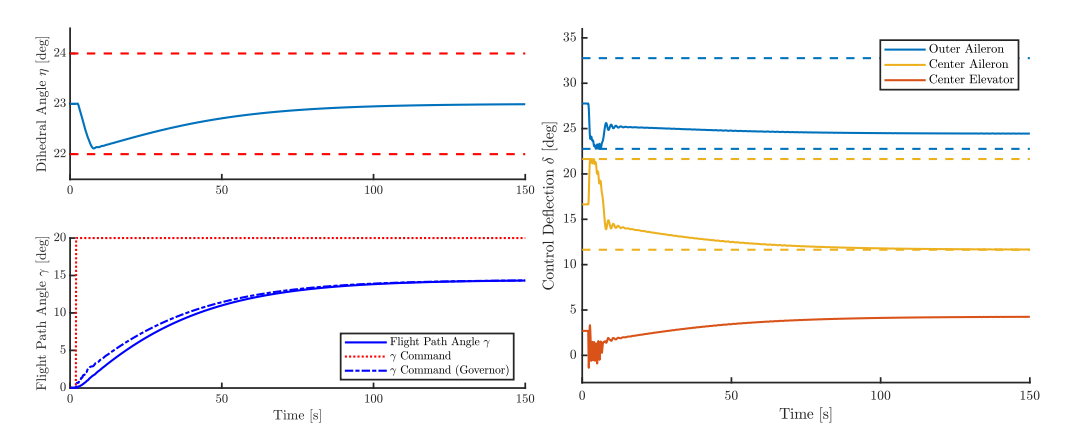


Fig. 12 ERG limits the system response to prevent going beyond constraint bounds by capping $\gamma = 14.33^{\circ}$, resulting in the center aileron lower bound being actively constrained.

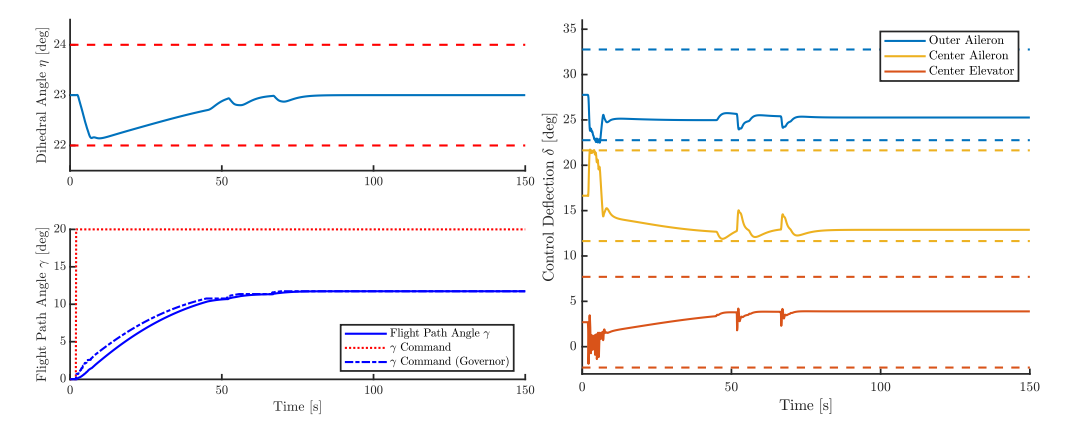


Fig. 13 SRG also limits the system response to prevent going beyond constraint bounds, but caps at a lower $\gamma = 11.74^{\circ}$ and does not have any active nonlinear system constraints due to system mismatch.

As before, this behaves better than the corresponding SRG due to the divergence between the linear and nonlinear responses, as in the SRG response in Fig. 13.

The SRG has a limit of $\gamma = 11.74^{\circ}$, preventing the system from going beyond the constraint bounds, but has no constraints active at the final state at the end of the simulation. This is because the linear system's constraints are active,

but due to the mismatch between the linear and nonlinear systems, results in only the linear, and not the nonlinear, system not being actively constrained.

VII. Addition of Turbulence to the Controller Output

Adding in a simple turbulence model to the VFA model, as done in [8], where random velocities are added to the local velocity vectors of each of the three wing sections. This simulates variances in wind through these parameters. The random numbers are obtained from a normal, Gaussian, distribution with a standard deviation of 1 ft/s and a mean of 0 ft/s. These are added to each of the u_i and w_i for each of the three wing sections i, as in

$$\hat{u}_i = u_i + \mathcal{N}(0 \text{ft/s}, (1 \text{ft/s})^2),$$

 $\hat{v}_i = v_i,$ (46)
 $\hat{w}_i = u_i + \mathcal{N}(0 \text{ft/s}, (1 \text{ft/s})^2),$

where \hat{u}_i and \hat{w}_i are the new velocity values used in place of the original u_i and w_i in the modeling equations when the wind model is active and \mathcal{N} is a normal distribution. As turbulence is only added in the sectional \hat{x}_i and \hat{y}_i directions, \hat{v}_i is the same as before. This is due to the longitudinal model, in which v_2 must be 0, and the disturbances on sections 1 and 3 are symmetrical in order to remain within the longitudinal plane. For the ERG, we first use predictions for the DSM obtained without the wind disturbance in the model; however, the last state that is obtained from the simulation is used in the modeling of the ERG, and so the ERG still must account for an initial value of disturbance when propagating the system forward in time. When we run these simulations, the ERG is still able to perform well, providing responses that still generally prevent constrained region excursions. For example, Fig. 14 shows the first case, $\eta = 5^{\circ}$ and $\gamma = 5^{\circ}$, where the ERG is successfully able to prevent large deviations from the constraints and maintain the desired γ .

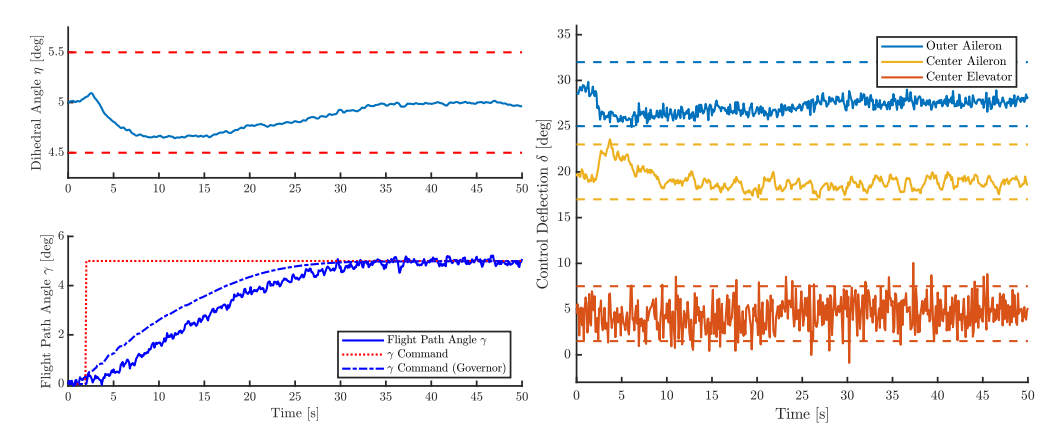


Fig. 14 ERG is able to maintain the stability of the system during the random disturbances while preventing large exceedances in the control parameters despite added turbulence model.

In the case as above where we do not include a wind disturbance in the prediction model for the ERG when calculating \dot{v} , the controller reaches a steady state where the average disturbance is right on the constraint line, meaning that we are continuously moving out of the constrained region. To illustrate this, we look at a simulation with $\eta = 23^{\circ}$, target $\gamma = 20^{\circ}$, and the constraints are

$$22^{\circ} \le \eta \le 24^{\circ}, -35^{\circ} \le \delta_{e_c} \le 30^{\circ}, -35^{\circ} \le \delta_{a_o} \le 30^{\circ}, 10^{\circ} \le \delta_{a_c} \le 20^{\circ}.$$
 (47)

As before, the turbulence standard deviation is 1 ft/s. In Fig. 15, simply propagating the system forward, while constraining the simulation before reaching the desired $\gamma=20^\circ$, does not adequately prevent δ_{a_c} from moving below its 10° lower limit. This is because this ERG formulation does not include the turbulence disturbance in the ERG prediction simulation. Thus, on average, the mean disturbance is 0 ft/s, and so after enough time the simulation tracks towards the $\gamma=17.58^\circ$ obtained from the case with no wind disturbance.

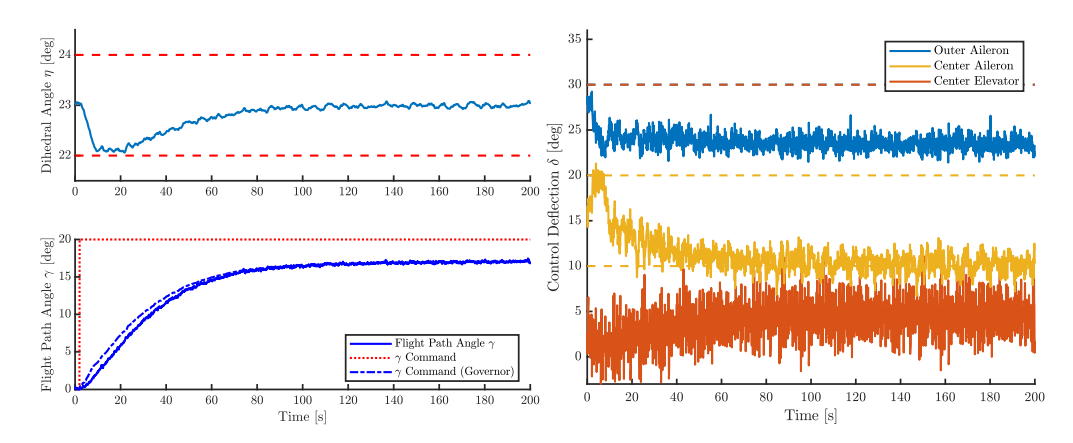


Fig. 15 ERG without the wind included in the prediction simulation cannot adequately prevent the center aileron from moving beyond lower constraint limit.

Adjusting the model to include this wind in the prediction simulation provides much more favorable results in Fig. 16. The ERG caps the flight path angle at about $\gamma = 14^{\circ}$, much lower than before, and successfully prevents the large constraint violations from Fig. 15.

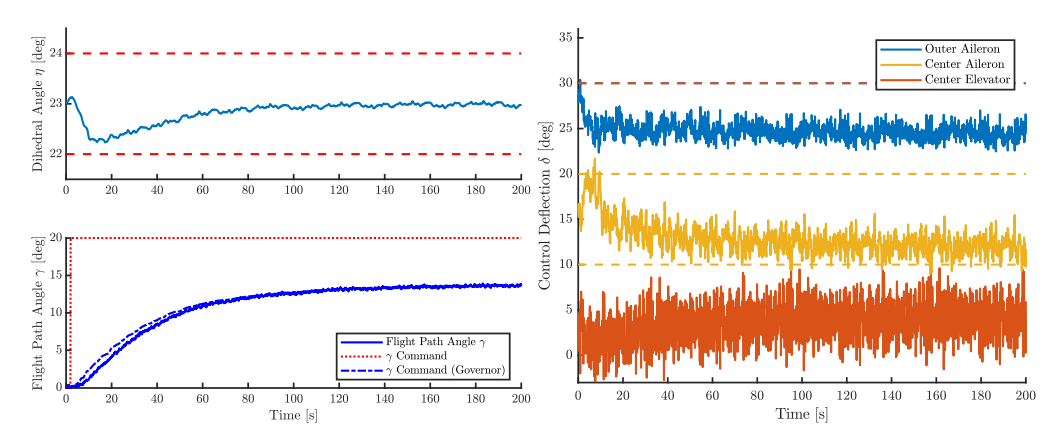


Fig. 16 ERG with the wind included in the prediction simulation prevents most excursions beyond the lower constraint limit for the center aileron.

VIII. Conclusion

An LQ-I controller in combination with an ERG was presented that shows this control scheme is effective for the control of a multibody aircraft in longitudinal flight, based on the aircraft model provided by [7]. This control scheme provides good performance in constrained control, and can act well even as the nonlinear and linear models diverge, providing better performance than a similar SRG, and helps to stabilize a system that would otherwise be unstable due to the control surface deflections that would otherwise be requested by the LQ-I controller alone. Furthermore, this control method can provide constrained control even under the case of a stochastic turbulence model. Additional studies would be needed on higher-order models that cover more of the dynamics, not just longitudinal dynamics, to assess the effectiveness of this controller under conditions closer to those that would be seen in a real-world aircraft.

Acknowledgments

This work was partially supported by the FNRS MIS project "Optimization-free Control of Nonlinear Systems subject to Constraints," Ref. F452617F and by the National Science Foundation Award Numbers ECCS-1931738 and CMMI-1904394.

We would like to thank Dr. Travis Gibson for providing the VFA model from [7] and assistance in its use.

References

- [1] Kopf, M., Bullinger, E., Giesseler, H.-G., Adden, S., and Findeisen, R., "Model Predictive Control for Aircraft Load Alleviation: Opportunities and Challenges," *Proceedings of American Control Conference*, 2018, pp. 2417–2424.
- [2] Haghighat, S., T. Liu, H. H., and RA Martins, J. R., "Model-predictive gust load alleviation controller for a highly flexible aircraft," *Journal of Guidance, Control, and Dynamics*, Vol. 35, No. 6, 2012, pp. 1751–1766.
- [3] Shearer, C. M., and Cesnik, C. E., "Trajectory Control for Very Flexible Aircraft," *AIAA Journal of Guidance, Control, and Dynamics*, Vol. 31, No. 2, 2008, pp. 340–357.
- [4] Dillsaver, M., Cesnik, C. E., and Kolmanovsky, I., "Trajectory Control of Very Flexible Aircraft with Gust Disturbance," *AIAA Atmospheric Flight Mechanics (AFM) Conference*, 2013. doi:10.2514/6.2013-4745, URL https://arc.aiaa.org/doi/abs/10.2514/6.2013-4745.
- [5] Gonzalez, P. J., Silvestre, F. J., Paglione, P., Köthe, A., Pang, Z. Y., and Cesnik, C. E., "Linear Control of Highly Flexible Aircraft based on Loop Separation," *AIAA Atmospheric Flight Mechanics Conference*, 2016. doi:10.2514/6.2016-3398, URL https://arc.aiaa.org/doi/abs/10.2514/6.2016-3398.
- [6] Dillsaver, M. J., Kalabic, U. V., Kolmanovsky, I. V., and Cesnik, C. E. S., "Constrained control of very flexible aircraft using reference and extended command governors," *Proceedings of American Control Conference*, 2013, pp. 1608–1613.
- [7] Gibson, T., Annaswamy, A., and Lavretsky, E., "Modeling for Control of Very Flexible Aircraft," *AIAA Guidance, Navigation, and Control Conference*, 2011. doi:10.2514/6.2011-6202, URL https://arc.aiaa.org/doi/abs/10.2514/6.2011-6202.
- [8] Gibson, T. E., "Closed-loop Reference Model adaptive control: with application to very flexible aircraft," Ph.D. thesis, Massachusetts Institute of Technology, 2014.
- [9] O'Rourke, I., Kolmanovsky, I., and Girard, A., "Scalar Reference Governor for Constrained Maneuver and Shape Control of Nonlinear Multibody Aircraft," *Proceedings of IFAC Symposium on Nonlinear Control Systems*, 2019 (to be published).
- [10] Kolmanovsky, I., Garone, E., and Cairano, S. D., "Reference and command governors: A tutorial on their theory and automotive applications," *Proceedings of 2014 American Control Conference*, 2014, pp. 226–241.
- [11] Garone, E., Cairano, S. D., and Kolmanovsky, I., "Reference and command governors for systems with constraints: A survey on theory and applications," *Automatica*, Vol. 75, 2017, pp. 306 328.
- [12] Nicotra, M. M., and Garone, E., "The Explicit Reference Governor," *IEEE Control Systems Magazine*, Vol. 38, 2018, pp. 89 107.
- [13] Nicotra, M. M., and Garone, E., "Explicit Reference Governor for Constrained Nonlinear Systems," *IEEE Transactions on Automatic Control*, Vol. 61, 2016, pp. 1379 1384.